Article | Open Access

Energy Materials

Li *et al. Energy Mater.* **2026**, *6*, 600152 **DOI:**10.20517/energymater.2026.231

Rational design of multifunctional pseudohalide anions for synergistic defect passivation and suppressed ion migration in perovskite solar cells

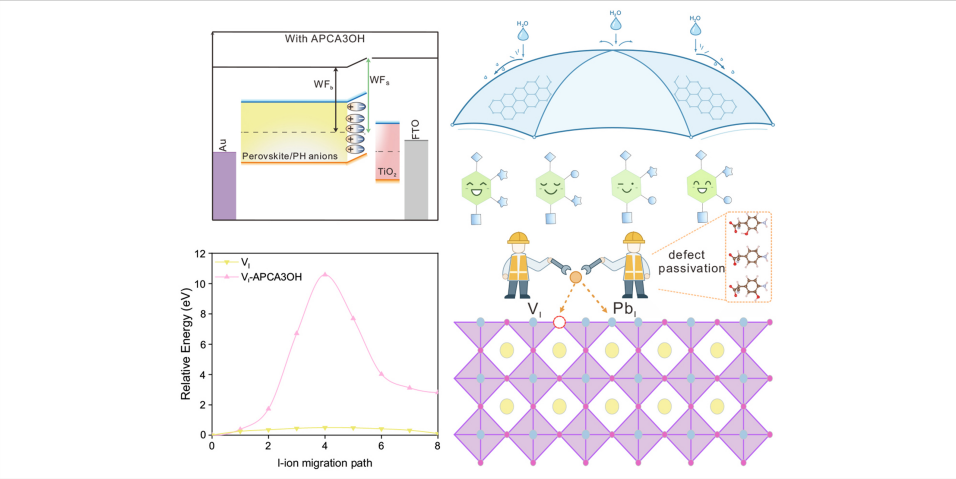
Nan Li[1], Ping-Ping Sun[1,*], Haiying Zhang[1], Zhixuan Peng[1], Qin Ding[1], Beibei Zhang[1], Jiayi Huang[1], Chaoyuan Zeng[1,*], Qinxi Dong[1,2,*], Weijie Chi[1,*]

Keywords:
Perovskite solar cells, defect passivation, multifunctional pseudohalide anions, first-principles calculations, molecular dynamics

Citation: Li, N.; Sun, P. P.; Zhang, H.; Peng, Z.; Ding, Q.; Zhang, B.; Huang, J.; Zeng, C.; Dong, Q.; Chi, W. Rational design of multifunctional pseudohalide anions for synergistic defect passivation and suppressed ion migration in perovskite solar cells. *Energy Mater.* **2026**, *6*, 600152. https://dx.doi.org/10.20517/energymater.2026.231

Received: 20 Jul 2026
First Decision: 21 Aug 2026
Revised: 10 Sep 2026
Accepted: 10 Oct 2026
Published: 4 Nov 2026

Academic Editor:
Soo Young Kim
Copy Editor:
Ping Zhang
Production Editor:
Ping Zhang



Abstract

To enhance both the efficiency and stability of perovskite solar cells (PSCs), an ideal interface needs to be formed; that is, defect passivation, efficient charge transport and suppression of ion migration must be achieved simultaneously. We rationally designed a series of multifunctional pseudohalide (PH) anions in this study, including APCA, APCA2OH, and APCA3OH, and systematically and synergistically regulated the interfacial properties by introducing functional groups such as -COO^-, -OH, -NH_2, -CN, and aromatic rings. First-principles calculations and *ab initio* molecular dynamics (AIMD) simulations indicate that the optimal APCA3OH molecule anchors to the perovskite surface via strong multidentate chelation. Cooperative coordination can reduce both deep and shallow trap states effectively by breaking up the harmful Pb_3 trimers and Pb_2 dimers associated with Pb-I antisite (Pb_I) and iodine vacancy (V_I) defects. From an electronic standpoint, the intrinsic dipole moments of the designed PH anions can adjust the surface work function to reduce the energy-level mismatch at the electron-selective contact and promote

[1]School of Chemistry and Chemical Engineering, Hainan University, Haikou 570228, Hainan, China.
[2]School of Transportation Civil Engineering, Shandong Jiaotong University, Jinan 250357, Shandong, China.

***Correspondence to:** Prof. Ping-Ping Sun, Prof. Chaoyuan Zeng, Prof. Weijie Chi, School of Chemistry and Chemical Engineering, Hainan University, Haikou 570228, Hainan, China. E-mail: pingpingsun@hainanu.edu.cn; zengchaoyuan@hainanu.edu.cn; weijie_chi@hainanu.edu.cn; Prof. Qinxi Dong, School of Chemistry and Chemical Engineering, Hainan University, Haikou 570228, Hainan, China; School of Transportation Civil Engineering, Shandong Jiaotong University, Jinan 250357, Shandong, China. E-mail: dongqinxi@hainanu.edu.cn

non-radiative carrier extraction. In addition, the synergistic chemical bonding and prominent steric hindrance caused by the ortho-hydroxyl group in APCA3OH increase the activation energy for iodide migration to 10.72 eV and thus inhibit halide diffusion. The functionalized structure also forms a dense hydrogen-bonding network that restricts water infiltration and enhances dynamic stability. By elucidating the structure-activity relationships of these complex molecular architectures, this work provides fundamental molecular insights for the design of comprehensive interfacial passivants for future perovskite photovoltaics.

INTRODUCTION

Single-junction perovskite solar cells (PSCs) based on organometallic halides have achieved a certified high power conversion efficiency (PCE) of 28%, comparable to that of commercial silicon solar cells (27.8%)[1]. Despite these remarkable advances, uncontrollable crystallization during the solution process leads to a high density of bulk and interfacial defects[2-4]. These defects generally involve uncoordinated atoms that can readily serve as nonradiative recombination centers and facilitate ion migration and structural degradation, thereby aggravating hysteresis and deteriorating device performance and lifetime[5-7]. Therefore, reducing defect formation is critical for improving the quality of perovskite films, which requires the development of advanced passivation strategies[8,9].

Small organic molecules have been studied as defect-passivating agents for PSCs, due to their adjustable physical and chemical properties[10-12]. Among them, monovalent pseudohalide (PH) anions (e.g., PF_6^-, BF_4^-, SCN^-, $HCOO^-$, CH_3COO^-) are frequently used to passivate defects, and, due to their ionic similarity to native halides, have shown good results. The above features can achieve several functions: strengthen the structure, regulate energy levels, reduce non-radiative recombination, and improve film crystallinity[13-17]. To further improve the defect passivation effect, some functional groups (such as -CN, C=O, -OH, $-NH_2$, aromatic rings, and halides) have been added to these ionic structures. The above structural modifications can regulate the crystal growth of the molecules and form specific chemical bonds with the perovskite lattice to reduce defect density and improve film morphology[18-21]. For example, Jeong *et al.* showed that adding formamidine formate to $FAPbI_3$-based PSCs reduced non-radiative recombination and improved device performance by iodide vacancy passivation and hydrogen bonding between $HCOO^-$ PH anions and FA^+ cations[22]. Based on the above molecular analysis, more research has been conducted to design multifunctional passivation molecules that can address various types of defect sites. The arrangement of functional groups and their cooperative effects are necessary to be optimized for passivation. For example, the optimized geometry of carbonyl (C=O) and amino ($-NH_2$) groups in caffeine and its derivatives effectively suppresses Pb antisite defects[23], and the symmetrical spatial arrangement of 5-amino-3-pyridinecarboxylic acid maximizes interactions with both halide ions and undercoordinated sites[24]. Similarly, highly functionalized molecules such as D-4-tert-butylphenylalanine with -COOH, $-NH_2$, a benzene ring[25,26], and 3-phenoxy-2-hydroxypropyl acrylate featuring -OH, C=O, benzene ring[27], have been developed to address multiple types of defects simultaneously. Li *et al.* have further promoted this idea by using the electron-rich oxygen atoms of a 1,2,2-tris(4-methoxyphenyl)ethene derivative to simultaneously anchor and passivate multiple uncoordinated defects[28]. Although there have been some good results, most of the multifunctional passivation molecules are still unknown[29]. More notably, the fundamental structure-activity relationships that control the optimal selection, combination, and space distribution of functional groups in complex molecular structures have not been systematically determined, and this is a serious problem for subsequent research[30-33].

To address this important knowledge gap and elucidate the structure-activity relationships in complex passivation systems, we rationally designed three structurally related multifunctional PH anions, namely APCA, APCA2OH and APCA3OH. These molecules share a common molecular framework containing

-COO^-, -OH, -NH_2, -CN, and a benzene ring. APCA is devoid of hydroxyl groups, whereas APCA2OH and APCA3OH each incorporate one hydroxyl group at different positions within the molecular framework. This molecular design minimizes variations in the molecular backbone while allowing systematic investigation of the effects of hydroxyl functionalization and its spatial position on the interfacial properties of the passivation molecules. In particular, the electron-rich -CN and -COO^- groups, coupled with the planar π-conjugated aromatic framework, provide potential Lewis-basic sites for coordinating with uncoordinated Pb^{2+} defects. Meanwhile, the introduced -OH group enables additional hydrogen-bonding interactions with the perovskite lattice and organic cations (e.g., MA^+), while the hydrophobic aromatic framework acts as a molecular barrier against water penetration, thereby improving the moisture resistance of the passivated interface. Therefore, these three molecules constitute a model molecular series for elucidating how hydroxyl functionalization and spatial arrangement regulate interfacial binding, defect passivation, and moisture resistance. Supported by first-principles calculations and *ab initio* molecular dynamics (AIMD) simulations, we found that the rationally designed PH anions tend to adopt multidentate chelating configurations to bridge adjacent Pb^{2+} defect sites. The unique molecular structures play a crucial role in determining the spatial electronic distribution and interfacial binding strength, which are closely associated with the observed defect passivation effects and reduced non-radiative recombination. Consequently, the appropriate incorporation of APCA3OH enhances defect formation energies, reduces trap-state density, suppresses detrimental ion migration, and potentially contributes to longer carrier lifetimes and better transport mobility. Finally, the spatial arrangement of functional groups within APCA-based PH anions enables the simultaneous passivation of diverse defect sites through efficient synergistic interactions, demonstrating the potential of targeted molecular design for enhancing the performance of perovskite photovoltaics.

COMPUTATIONAL METHOD

The computational models for all systems, including pristine, defective, and passivated $MAPbI_3$, were constructed using a three-layer PbI_2-terminated (001) slab. A 25 Å vacuum layer was introduced along the *z*-direction to suppress spurious interactions between periodic images, resulting in supercell dimensions of 12.6 × 12.6 × 42 $Å^3$ along the *x*, *y*, *z* directions, respectively. The geometries of the PH anions were optimized using Gaussian 16[34-36]. First-principles calculations were performed using Vienna *Ab initio* Simulation Package[37-39]. The exchange-correlation interactions were described using the generalized gradient approximation (GGA) with the Perdew-Burke-Ernzerhof (PBE) functional[40]. The projector augmented-wave (PAW) method[41] was employed to describe the interactions between the ionic cores and valence electrons. A plane-wave cutoff energy of 400 eV and an electronic convergence criterion of 10^{-5} eV were used throughout the calculations. The climbing-image nudged elastic band (CI-NEB) method[42,43] was used to calculate the iodide ion migration barriers, with a force convergence criterion of 0.15 eV $Å^{-1}$. The Grimme's D3 dispersion correction[44] was included to account for van der Waals (vdW) interactions. To evaluate the interfacial behavior and structural robustness under humid conditions, AIMD simulations were performed using the CP2K package. The PBE functional was combined with the DFT-D3 dispersion correction, together with Goedecker-Teter-Hutter (GTH) pseudopotentials and DZVP-MOLOPT-SR-GTH basis sets[45,46]. A plane-wave cutoff energy of 400 Ry was employed. The simulations were carried out in the canonical ensemble at 300 K using a Nosé-Hoover thermostat, with a time step of 1 fs for a total simulation time of 15 ps[47,48]. Time-dependent density functional theory (TDDFT) calculations were further performed using the CP2K package based on the structures obtained from the AIMD simulations. A plane-wave cutoff of 400 Ry and a relative cutoff of 50 Ry were employed for the electron-density representation, together with the DZVP-MOLOPT-SR-GTH basis set and the PBE exchange-correlation functional[45]. For each system, the lowest 50 singlet excited states were calculated, together with 30 additional virtual molecular orbitals for subsequent excited-state electronic-structure analysis. The convergence threshold for the TDDFT excitation energies was set to 1 × 10^{-4} eV, while the Self-Consistent Field convergence criterion was set to 1 × 10^{-5} eV[48,49].

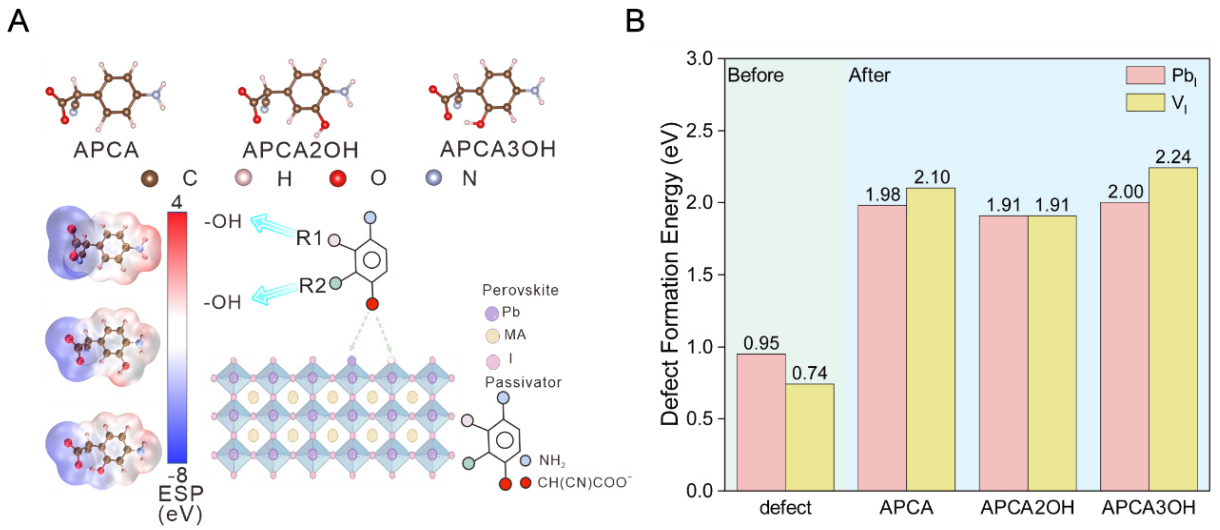


Figure 1. (A) Geometries and electrostatic potential diagrams of APCA, APCA2OH, APCA3OH, together with the schematic illustrations of their passivation on defective perovskite surface; (B) DFEs of the three PH anions before and after passivation. DFEs: Defect formation energies; PH: pseudohalide; ESP: electrostatic potential.

The defect formation energy (DFE) was calculated using[50,51]:

$$\Delta H = E_D - E_{D=0} + \sum_i n_i \mu_i \tag{1}$$

where E_D and $E_{D=0}$ represent the total energies of the defective and pristine $MAPbI_3$ slabs, respectively. n_i denotes the change in the number of atoms of element i associated with defect formation, and μ_i represents the corresponding chemical potential referenced to the most stable phase of element i. The iodine migration rate constant (κ) was estimated using the Arrhenius equation[52,53].

RESULTS AND DISCUSSION

Among various defect types, intrinsic point defects dominate due to their low defect formation energies (DFEs) and act as non-radiative recombination centers by introducing deep or shallow trap states, thereby severely affecting exciton recombination, charge-carrier transport, and overall device stability[54-56]. In $MAPbI_3$, the DFEs of four typical point defects, including iodine vacancy (V_I), Pb-I antisite defects (Pb_I), I-Pb antisite defects (I_{Pb}), and lead vacancies (V_{Pb}), were calculated under Pb-rich conditions on the PbI_2-terminated (001) surface. Among these defects, V_I and Pb_I exhibit the lowest DFEs, indicating their preferential formation during film processing and identifying them as the primary passivation targets in this work [Supplementary Figure 1]. The corresponding DFE values under I-rich conditions were also evaluated to investigate the defect stability under different chemical environments. As shown in Supplementary Figure 2, the average DFEs under I-rich conditions are higher than those under Pb-rich conditions. Notably, V_I and Pb_I under Pb-rich conditions are known to induce shallow and deep trap states, respectively. To synergistically passivate these two types of defects, three multifunctional PH anions based on 2-(4-aminophenyl)-2-cyanoacetate (APCA), namely APCA, APCA2OH, and APCA3OH [Figure 1A], were rationally designed. These molecules contain $-COO^-$, -OH, $-NH_2$, -CN, and benzene ring groups and were employed to investigate their surface passivation mechanisms under Pb-rich conditions.

Electrostatic potential (ESP) mapping of APCA reveals that the amino group attached to the benzene ring acts as an electron-donating moiety, facilitating hole transport similarly to conventional hole transport materials (HTMs)[57,58], whereas the para-cyanoacetate group functions as an electron-accepting moiety[59].

The integration of these acceptor (A) and donor (D) units generates a pronounced molecular dipole moment within the framework [Supplementary Figure 3]. To further evaluate the role of auxiliary functionalization, hydroxyl groups were introduced at the meta- and ortho-positions of the benzene ring, yielding APCA2OH and APCA3OH, respectively. ESP and molecular orbital analyses indicate that APCA3OH exhibits enhanced electron-withdrawing capability.

All three PH anions coordinate with the perovskite lattice at the terminal -COO^- group during the evaluation of host-guest interactions. By systematically simulating the binding configurations of each functional group at both Pb_I and V_I sites, the lowest-energy structures show strong multidentate chelation between the molecules and undercoordinated Pb atoms near the defects [Supplementary Figure 4], and an interfacial dipole is formed that points from the PH anions towards the perovskite surface. Specifically, at the V_I surface, either a single oxygen atom from the C=O group or multiple oxygen atoms from both the C=O and -OH groups occupy the vacancy site through steric hindrance to form strong Pb-O chemical bonds. This cooperation will help to improve the form of the film in post-production. After molecular anchoring, the DFEs of the passivated systems are significantly higher than those of the corresponding unpassivated system [Figure 1B], and thus the surface has improved thermodynamic stability. Stabilization will suppress the formation of both V_I and Pb_I defects simultaneously and reduce non-radiative recombination. In addition, the polar groups (-COO^-, -OH, -CN) are located outside the benzene ring, and a good pathway for hole extraction and transport is formed. The charge density difference (CDD) and plane-averaged CDD profiles also show this interaction by presenting the spatial separation of electron and hole accumulation regions [Supplementary Figure 5]. Bader charge analysis shows that approximately 0.7 e^- is transferred to the PH anion. Furthermore, charge distribution extends into the perovskite lattice due to the combined effects of D-A molecular dipoles and Lewis acid-base interactions, regulating the surface energy levels and improving hole extraction efficiency[60].

Band structure analysis demonstrates that unpassivated Pb_I defects introduce deep trap states within the bandgap between the conduction band minimum (CBM) and valence band maximum (VBM), resulting in a bandgap of 1.74 eV [Figure 2A and Supplementary Table 1]. Density of states (DOS) analysis and contour plots further confirm that these localized trap states primarily originate from the p-orbitals of the defective Pb atoms [Supplementary Figures 6A and 7]. In contrast, the V_I defect narrows the bandgap to 1.55 eV without introducing mid-gap trap states [Figure 2B and Supplementary Table 1], while exhibiting orbital contributions to the conduction and valence bands similar to those of the Pb_I-defective surface [Supplementary Figures 6B and 8]. Upon passivation, the trap states on the Pb_I surface are substantially suppressed, while the bandgap of the V_I surface is widened to values comparable to those of the Pb_I system. After passivation with APCA, APCA2OH and APCA3OH, the bandgaps of the V_I defect system increase to 1.72, 1.73 and 1.75 eV, respectively [Figure 2C-H and Supplementary Table 1]. For narrow-bandgap perovskite materials, moderate bandgap widening can favor an increase in open-circuit voltage (V_{OC}), thereby contributing to improved photovoltaic performance. The V_I defect induces anomalous bandgap narrowing by introducing defect-related states and perturbing the electronic structure near the band edges. Upon passivation with PH anions, these defect-induced states are effectively suppressed, thereby reducing their contribution to non-radiative recombination and restoring the band-edge electronic structure. Such suppression of defect states and recovery of the band-edge electronic structure are therefore favorable for reducing V_{OC} losses and achieving a higher V_{OC}[61,62]. This convergence in electronic structure is also reflected in the optical absorption spectra, which exhibit consistent spectral shifts without compromising the absorption strength [Supplementary Figure 9]. These results indicate that all three PH anions provide synergistic passivation and yield similar electronic-structure characteristics across different defect systems, leading to comparable passivation effects for multiple defect types. The DOS profiles further confirm that the PH anions do not perturb the orbital contributions near the band edges, indicating that no additional trap

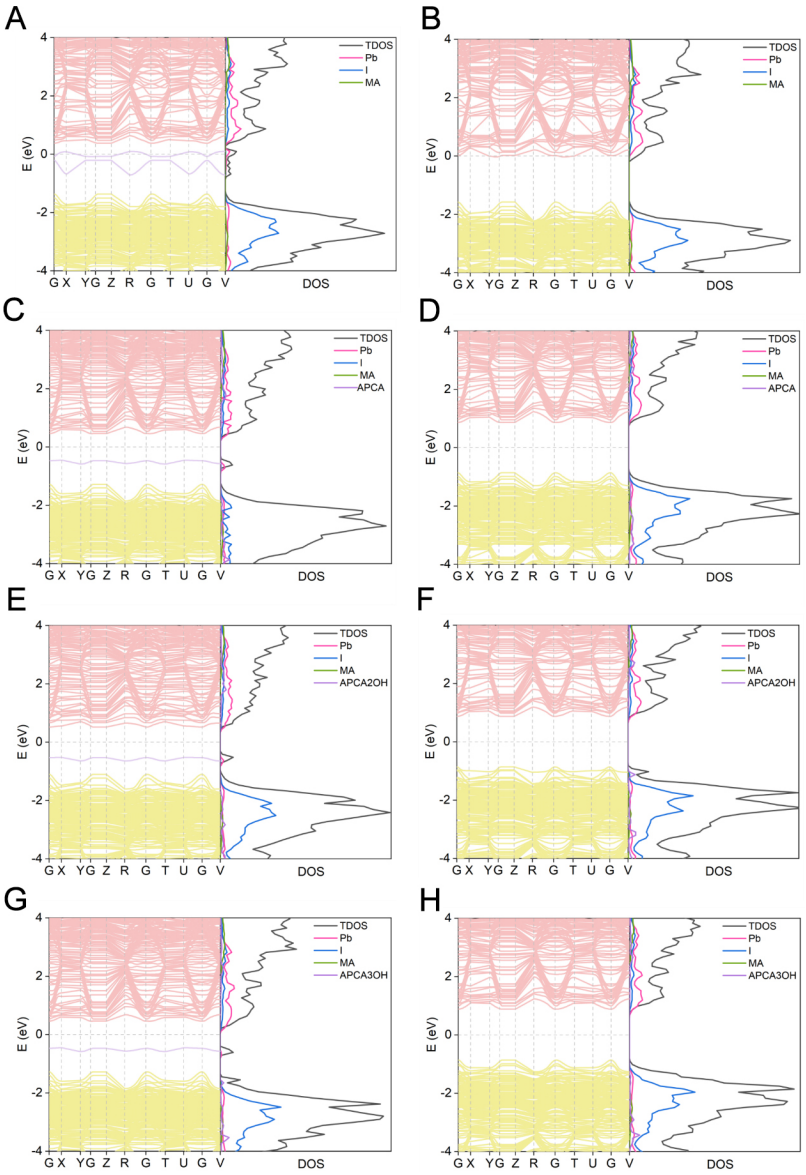


Figure 2. Band structures and DOS of (A) Pb_I_$MAPbI_3$, (B) V_I_$MAPbI_3$, (C) APCA@Pb_I_$MAPbI_3$, (D) APCA@V_I_$MAPbI_3$, (E) APCA2OH@Pb_I_$MAPbI_3$, (F) APCA2OH@V_I_$MAPbI_3$, (G) APCA3OH@Pb_I_$MAPbI_3$, and (H) APCA3OH@V_I_$MAPbI_3$. DOS: Density of states; TDOS: total density of states; MA: methylammonium.

states are introduced [Supplementary Figure 6C-H]. Nevertheless, in the PH@Pb_I_$MAPbI_3$ systems, the residual trap states exhibit flat band characteristics, with localized charge largely removed from the defective Pb site. The resulting charge distribution resembles the CBM contribution of the pristine system, indicating substantially weakened carrier trapping [Supplementary Figure 7]. In addition, the VBM contour plots exhibit similar distributions across all systems, with the charge density extending throughout the entire structure, including the PH anions. This distribution indicates that, after electron excitation to the CBM, the remaining holes are delocalized across the structure, suggesting that these PH anions can effectively facilitate hole extraction and subsequent transport toward the HTMs [Supplementary Figures 7-8].

To investigate the structural origin of the substantial reduction in trap states at the Pb_I defective surface and the bandgap widening of the V_I defective surface after adding PH anions, local atomic configurations were studied. In the unpassivated Pb_I system, a Pb_3 trimer exists at the defect site and serves as the structural unit

for the formation of deep trap states [Supplementary Figure 10A]. The corresponding trap-state contour plot also shows that the charge density is concentrated around the Pb_3 trimer [Supplementary Figure 7A]. Passivation by PH anion effectively disrupts the Pb_3 trimer and relaxes the local structure into a less harmful Pb_2 dimer configuration [Supplementary Figure 10B-D], thus significantly reducing the trap states [Supplementary Figure 7B-D]. The structure reconstruction shows that residual trap states still exist in the band structure, but they have been reduced significantly after passivation [Figure 2C, E and G]. For the V_I defect, the lack of iodine leads to the formation of a Pb_2 dimer; thus, there is significant distortion of the inorganic octahedral framework and a narrowing of the bandgap [Supplementary Figure 11A]. Passivation eliminates the Pb_2 dimer and, at the same time, oxygen atoms from the -COO^- group occupy the vacant iodine sites to form strong Pb-O bonds. These interactions restore the distorted octahedral framework to its original shape [Supplementary Figure 11B-D] and thus increase the bandgap. In addition, comparison of the passivated structures on the Pb_I and V_I-defective surfaces [Supplementary Figures 10B-D and 11B-D] shows that they have a high degree of structural integrity and atomic arrangement. This structural similarity indicates that the PH anions produce comparable passivation effects on the two distinct defect types and explains why the two defective surfaces exhibit similar bandgap values after passivation.

Beyond localized defect healing, we further evaluated the macroscopic effects of passivation on device energetics and carrier transport. The electron-hole pair creation energy (W) is an important parameter for evaluating electron-hole pair generation and the internal quantum yield η[63-66]. The W values of all passivated structures differ only slightly from one another [Supplementary Figure 12], further indicating that these PH anions can enhance the photo-response and charge transport. Energy-level alignment analysis reveals that the PH anions modulate the surface work function (WF) through their intrinsic dipole moments [Figure 3A and B]. The net positive dipoles increase the built-in potential at the interface [Supplementary Figures 3A and 13], an effect mainly arising from the highly polar -CH(CN)COO^- and -OH terminal groups. This resulting enhancement of the interfacial electric field across the perovskite/electron transport material (ETM) (TiO_2) interface reduces the energy-level offsets [Figure 3C and D], while the more consistent alignment of the energy cutoffs facilitates rapid carrier extraction and suppresses V_{OC} loss[67]. Notably, APCA3OH provides more favorable energy-level alignment on both defective surfaces than APCA2OH and APCA. This alignment promotes electron transfer to ETMs and hole transfer to HTMs, thereby effectively reducing V_{OC} loss.

Effective mass calculations further suggest a predicted trend of improved carrier-transport characteristics. According to deformation potential (DP) theory, the effective mass is an important parameter governing carrier transport, and carrier mobility is inversely related to the effective mass[68,69]. When the other relevant parameters, including the elastic constant and deformation potential constant, are comparable, a smaller effective mass favors more efficient carrier transport. We therefore calculated the electron and hole effective masses for all investigated systems. The electron effective masses increase substantially from 0.35 m_0 for pristine $MAPbI_3$ to 0.81 m_0 and 1.20 m_0 for Pb_I_$MAPbI_3$ and V_I_$MAPbI_3$, respectively. Meanwhile, the hole effective mass of Pb_I_$MAPbI_3$ increases from 0.29 m_0 to 0.48 m_0, whereas that of V_I_$MAPbI_3$ remains nearly unchanged. These changes indicate that defect formation impairs carrier transport by increasing the effective masses and enhancing carrier localization. Together with the emergence of defect-induced electronic states, these effects can further promote nonradiative recombination. After passivation with the three PH anions, the electron effective masses decrease in all defective systems. For holes, the effective mass of APCA@V_I_$MAPbI_3$ remains nearly unchanged at 0.29 m_0, whereas those of the other passivated systems decrease. Overall, these changes indicate that PH anion passivation generally improves carrier-transport characteristics while suppressing defect-induced carrier localization and nonradiative recombination. Moreover, due to its lowest hole effective mass, APCA3OH is expected to exhibit better hole transport properties on both defective surfaces [Figure 3E and F].

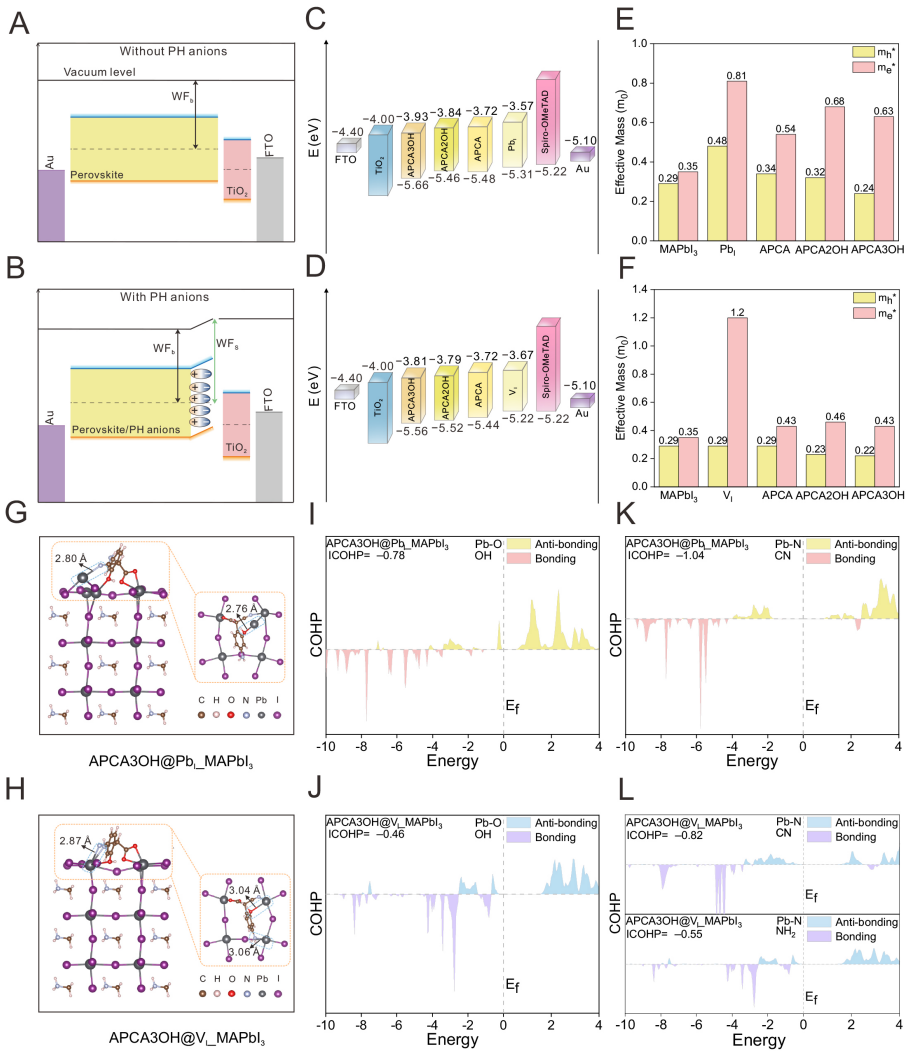


Figure 3. Simulated energy-level and work function diagrams of the surfaces (A) before and (B) after PH anion passivation. Energy-level alignment of the (C) Pb_I and (D) V_I defective systems before and after PH anion passivation within the complete device architecture; Electron and hole effective masses of the pristine, defective, and PH-anion-passivated systems for (E) Pb_I and (F) V_I defects; Interactions between the APCA3OH PH anion and surface Pb atoms on the defective surfaces of (G) Pb_I_$MAPbI_3$ and (H) V_I_$MAPbI_3$; COHP analysis of the Pb-O interactions in (I) APCA3OH@Pb_I_$MAPbI_3$ and (J) APCA3OH@V_I_$MAPbI_3$, and the Pb-N interactions in (K) APCA3OH@Pb_I_$MAPbI_3$ and (L) APCA3OH@V_I_$MAPbI_3$. PH: Pseudohalide; WF: work function; COHP: crystal orbital Hamilton population; ICOHP: integrated COHP; FTO: fluorine-doped tin oxide.

The superior electronic performance of APCA3OH relative to the other two PH anions can be attributed to its stable interfacial coupling network. The optimized structures show that APCA3OH binds to the perovskite surface through multidentate coordination. In addition to the primary -COO^- coordination, the auxiliary -CN, -OH, and -NH_2 groups form additional Pb-N, Pb-O, and H-I interactions that further stabilize the interfacial structure [Figure 3G and H]. Crystal orbital Hamilton population (COHP) analysis further confirms these interactions [Figure 3I-L]. Pb-O coordination involving the ortho-hydroxyl group gives large negative integrated COHP (ICOHP) values of -0.78 and -0.46 eV for Pb_I and V_I surfaces, respectively, indicating strong stabilizing interactions below the Fermi level [Figure 3I-J]. Furthermore, Pb-N coordination involving the -CN group gives ICOHP values of -1.04 eV and -0.82 eV for Pb_I and V_I surfaces, respectively. Pb-N coordination involving the -NH_2 group is also observed on the V_I surface, with an ICOHP value of -0.55 eV. These large negative ICOHP values clearly confirm that cooperative multisite anchoring promotes robust thermodynamic adsorption[70].

To elucidate the microscopic origin of the suppressed nonradiative recombination upon passivation, we employed TDDFT to investigate the effect of APCA3OH passivation on the excited-state behavior of defective $MAPbI_3$. Combined with quantitative hole-electron analysis, the spatial distribution of photoexcited carriers was further examined. As shown in Supplementary Figure 14, both the CBM and VBM of the unpassivated defective systems exhibit pronounced localization around the defect regions, indicating that the defect-related states participate in low-energy electronic excitations. Upon APCA3OH passivation, the localization of the frontier orbitals around the defect sites is substantially reduced, while their distributions become predominantly concentrated on the perovskite framework. This redistribution weakens defect-induced carrier localization and is expected to facilitate the delocalization and transport of photoexcited carriers[71].

The excited-hole, excited-electron, and CDD distributions provide further insight into the spatial separation and redistribution of photoexcited carriers upon passivation, offering microscopic evidence for the suppression of defect-assisted nonradiative recombination. As shown in Figure 4A, the excited-hole and excited-electron distributions in the Pb_I-defective system exhibit pronounced spatial overlap and are mainly localized near the perovskite surface. The corresponding CDD distribution further shows that the electron-density redistribution is primarily concentrated around the defect and neighboring regions, suggesting substantial involvement of the defect states in the photoexcitation process. Upon APCA3OH passivation [Figure 4B], the hole and electron distributions become more spatially separated, accompanied by a pronounced reduction in carrier localization around the defect region. Meanwhile, the CDD distribution reveals a redistribution of the excited-state charge density from the defect-related regions toward the perovskite framework, indicating that APCA3OH effectively regulates photoinduced charge redistribution and suppresses defect-induced carrier trapping. Similar behavior is observed in the V_I defective system [Figure 4C and D], where APCA3OH passivation redistributes the excited-state charge density and reduces carrier localization around the defect-related regions.

The favorable electronic properties of APCA3OH-passivated defective $MAPbI_3$ are further supported by quantitative excited-state hole-electron descriptors. As summarized in Supplementary Table 2, APCA3OH passivation decreases the hole-electron distribution overlap function (S_m) while increasing the electron-hole centroid distance (D_{ij}), indicating reduced spatial overlap and enhanced separation between photoexcited electrons and holes. This enhanced spatial separation is expected to reduce the probability of electron-hole recombination and facilitate the effective transport of photogenerated carriers. In addition, the decreased hole delocalization index (HDI) and electron delocalization index (EDI) indicate greater spatial delocalization of the excited-state holes and electrons, resulting in a more homogeneous charge distribution. The enhanced charge delocalization is expected to further reduce the likelihood of defect-assisted nonradiative recombination, highlighting the effectiveness of APCA3OH in regulating the excited-state charge distribution and electron-hole interactions[49,71].

Overall, the TDDFT results indicate that APCA3OH surface passivation effectively mitigates defect-induced carrier localization and enhances the spatial separation of photoexcited electrons and holes, thereby reducing the likelihood of defect-assisted nonradiative recombination and carrier trapping. These favorable excited-state characteristics are expected to promote the transport and utilization of photo-generated carriers and provide favorable conditions for extending carrier lifetime[72,73].

It is well established that V_I defects can facilitate halide-ion migration under operational conditions[74,75]. CI-NEB calculations reveal a low migration activation energy (E_a = 0.49 eV) and a high migration rate constant (κ)[42,43] of 2.30 × 10^5 s^{-1} for the unpassivated V_I surface [Supplementary Table 3, Figure 5A and B]. Such facile iodide migration can induce lattice distortion, interfacial degradation, phase segregation, V_{OC} loss, impaired

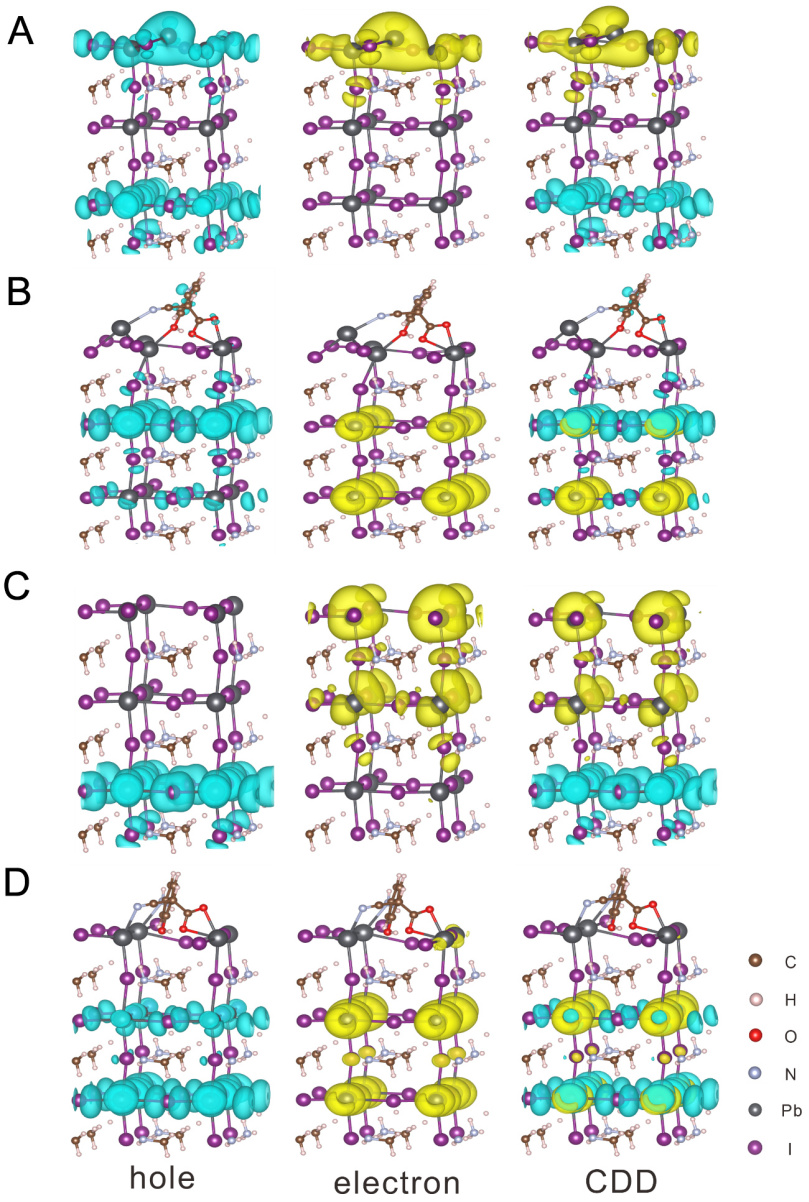


Figure 4. Spatial distributions of the excited-state hole, electron, and CDD calculated by TDDFT for (A) Pb_I_$MAPbI_3$, (B) APCA3OH@Pb_I_$MAPbI_3$, (C) V_I_$MAPbI_3$, and (D) APCA3OH@V_I_$MAPbI_3$. For each system, the left, middle, and right columns represent the spatial distributions of the hole, electron, and CDD, respectively, where CDD is defined as the electron density minus the hole density. The cyan and yellow isosurfaces represent the hole and electron densities, respectively. CDD: Charge density difference; TDDFT: time-dependent density functional theory.

charge extraction, and the formation of shallow trap states[76,77]. Moreover, accelerated iodide migration can enhance electron-phonon coupling and shorten carrier lifetimes, further deteriorating the optoelectronic performance of the perovskite. Meanwhile, iodine vacancies can serve as preferential adsorption sites for environmental H_2O and O_2 [Supplementary Figure 15], facilitating surface reactions and accelerating degradation of the perovskite lattice. Together, these effects compromise the long-term structural and environmental stability of perovskite materials[76,77]. Passivation markedly increases E_a to 5.4 eV for APCA, 5.8 eV for APCA2OH, and 10.72 eV for APCA3OH, thereby reducing κ to 7.55×10^{-78} s^{-1}, 1.44×10^{-84} s^{-1}, and 3.21×10^{-167} s^{-1}, respectively, and effectively suppressing the migration pathway [Supplementary Table 3, Figure 5A and B]. These results demonstrate that PH anion passivation strongly inhibits iodide migration and enhances structural stability. Analysis of the migration pathways from the initial state (IS) through the

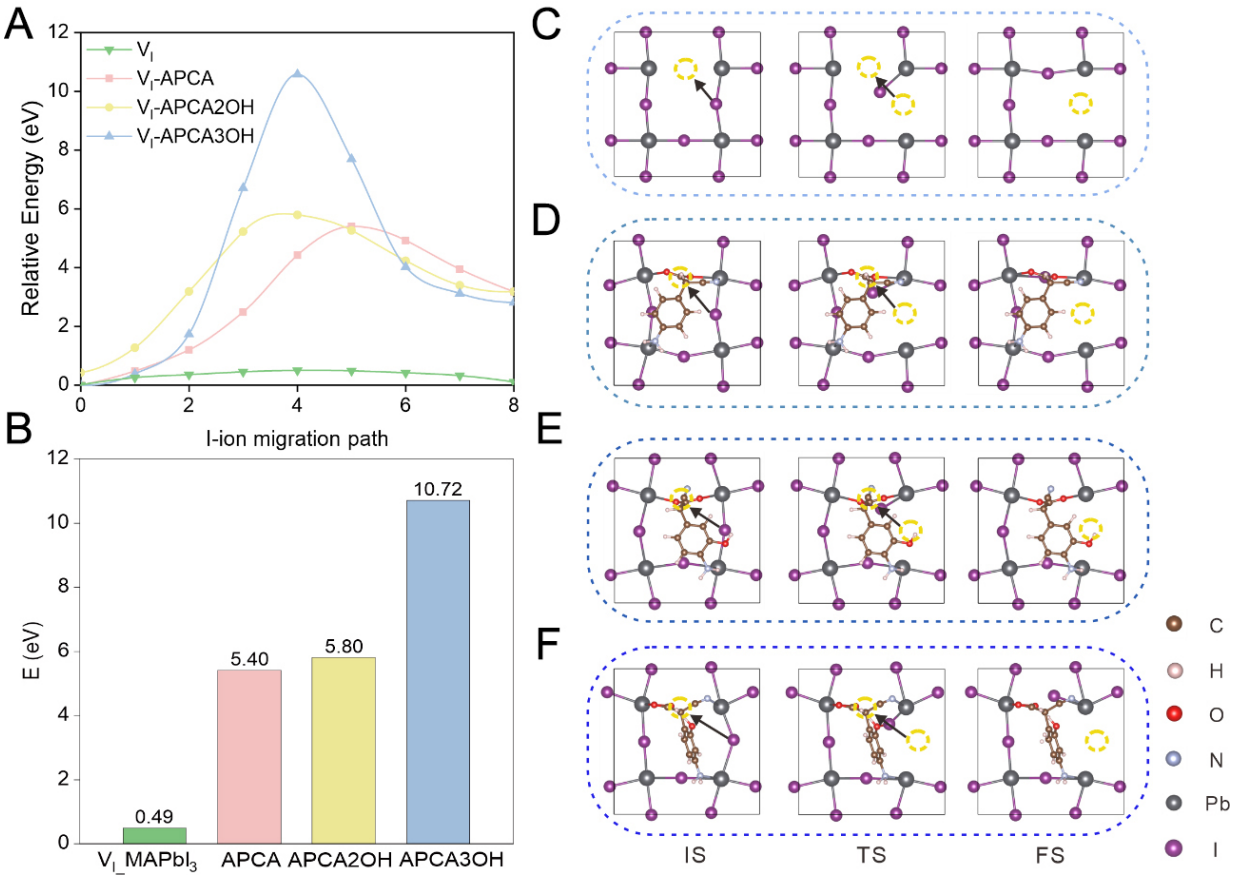


Figure 5. Inhibition of iodide ion migration in V_I_$MAPbI_3$ by different PH anions. (A) Transition-state energy profiles for iodide migration in different systems; (B) Activation energy (E_a) of the corresponding systems; Top views of the IS, TS, and FS along the iodide migration pathways on the surfaces of (C) V_I_$MAPbI_3$, (D) APCA@V_I_$MAPbI_3$, (E) APCA2OH@V_I_$MAPbI_3$, and (F) APCA3OH@V_I_$MAPbI_3$. PH: Pseudohalide; IS: initial state; TS: transition state; FS: final state.

transition state (TS) to the final state (FS) further elucidates the mechanism underlying the suppression of iodide migration [Figure 5C-F]. In the APCA3OH-passivated system, strong Pb-O, Pb-N and O-H interactions act together with steric hindrance to restrict iodide migration. At the TS, the migrating iodide ion must overcome strong repulsive interactions with oxygen atoms that tightly coordinate to the vacancy region through Pb-O bonds [Supplementary Figure 16]. Because the newly formed Pb-O bonds (~2.6 Å) are considerably shorter and stronger than the native Pb-I bonds (~3.3 Å), displacement of the passivant is energetically unfavorable.

The differences in E_a among the three PH anions can be further understood from their distinct coordination environments. As shown in Figure 5B, APCA and APCA2OH exhibit similar E_a values because both PH anions passivate the defect site through multiple interactions involving the same functional groups, namely -COO-, -CN, and -NH_2, where steric confinement further increases the migration barrier. In contrast, the substantially higher E_a of APCA3OH can be attributed to its ortho-hydroxyl group, which forms additional Pb-O bonds and further saturates the local coordination environment, thereby imposing a much higher kinetic barrier to iodide migration [Supplementary Figure 16]. The combined effects of spatial confinement and chemical anchoring more effectively hinder Pb-I bond reformation and suppress iodide migration. Importantly, both the presence and position of the -OH functional group play key roles in regulating structural stability and suppressing iodine migration.

The perovskite lattice is susceptible to degradation upon exposure to water and oxygen[78]. AIMD simulations were performed using CP2K for 15 ps at 300 K to evaluate the dynamic stability of the passivated surfaces against water intrusion[45,79,80]. In these simulations, four H_2O molecules were initially placed approximately 9 Å above the defective and passivated surfaces [Supplementary Figures 17-19]. The heights of the H_2O molecules exhibit pronounced fluctuations on the defective surfaces, with most molecules accumulating near the surfaces before penetrating into the perovskite octahedral cages [Figure 6A and B]. Trajectory snapshots show that structural collapse of both the Pb_I and V_I defective structures begins within 5 ps, followed by deep H_2O intrusion into the lattice by 10 ps [Supplementary Figure 20]. In stark contrast, all PH-passivated structures maintain stable energy and temperature profiles throughout the simulations [Supplementary Figures 21-22]. The H_2O molecules remain at substantially greater heights above both passivated defect surfaces; although some aggregation occurs, the molecules stay far from the surfaces [Figure 6C-H and Supplementary Figure 23]. Trajectory snapshots further show that the multifunctional groups form a dense hydrogen-bonding network that physically impedes moisture penetration, maintaining H_2O molecules at substantially greater distances from the perovskite surface. Accordingly, all passivated structures remain intact without evident structural deformation or damage [Supplementary Figures 24 and 25]. These AIMD results demonstrate that all three PH anions provide synergistic passivation of multiple defects. Among them, APCA3OH affords the strongest dynamic protection, completely preventing water penetration across the approximately 5 Å threshold.

Moreover, as noted above, a Pb_3 trimer and a Pb_2 dimer are present in the Pb_I and V_I defective structures, respectively. During the AIMD simulations, analysis of the Pb-Pb distance reveals distinct structural evolution for the two defective surfaces. The Pb-Pb distance profiles over the entire simulation further confirm that both types of defective structures tend to form stable Pb_2 dimers [Supplementary Figures 26 and 27]. These dimers seriously distort and disrupt the octahedral cages, leading to H_2O penetration and the release of organic cations [Supplementary Figure 28]. By contrast, in PH-anion-passivated Pb_I defect structures, the Pb-Pb distances remain essentially unchanged throughout the simulations, indicating that the Pb_3 trimer does not regenerate and that the resulting Pb_2 configuration remains structurally stable after passivation [Supplementary Figure 26]. In the passivated V_I-defective structures, the Pb-Pb distances increase to large values, indicating dissociation of the Pb_2 dimer while the integrity of the octahedral framework is preserved [Supplementary Figure 27]. These structural changes effectively eliminate the associated trap states, thereby reducing nonradiative recombination and supporting long-term operational stability. Overall, these AIMD results demonstrate that PH anion passivation forms a stable multifunctional protective layer that effectively suppresses defect-induced lattice distortion and water penetration. Among the investigated molecules, APCA3OH exhibits the most pronounced overall passivation performance, highlighting its potential for stabilizing defective perovskite surfaces. From the perspective of experimental feasibility, we further propose a potential solution-phase synthetic route for APCA3OH involving the Pd-catalyzed α-arylation of ethyl cyanoacetate with an appropriately functionalized aryl bromide, followed by ester hydrolysis and subsequent transformations[77]. The detailed proposed synthetic pathway is illustrated in Supplementary Figure 29. These findings provide a molecular-level design strategy for developing more robust perovskite materials and suggest that APCA3OH-passivated perovskites may exhibit promising stability and photovoltaic performance in future experimental devices. Further experimental synthesis of APCA3OH and device-level evaluation will be valuable for validating its practical applicability.

CONCLUSION

In summary, this study demonstrates that achieving high efficiency and operational stability in perovskite solar cells relies critically on the construction of an optimum interface. Our comprehensive investigation indicates that an ideal interface should simultaneously satisfy three key and cooperative requirements: (1) effective passivation of surface defects and thermodynamic stabilization of the perovskite surface structure;

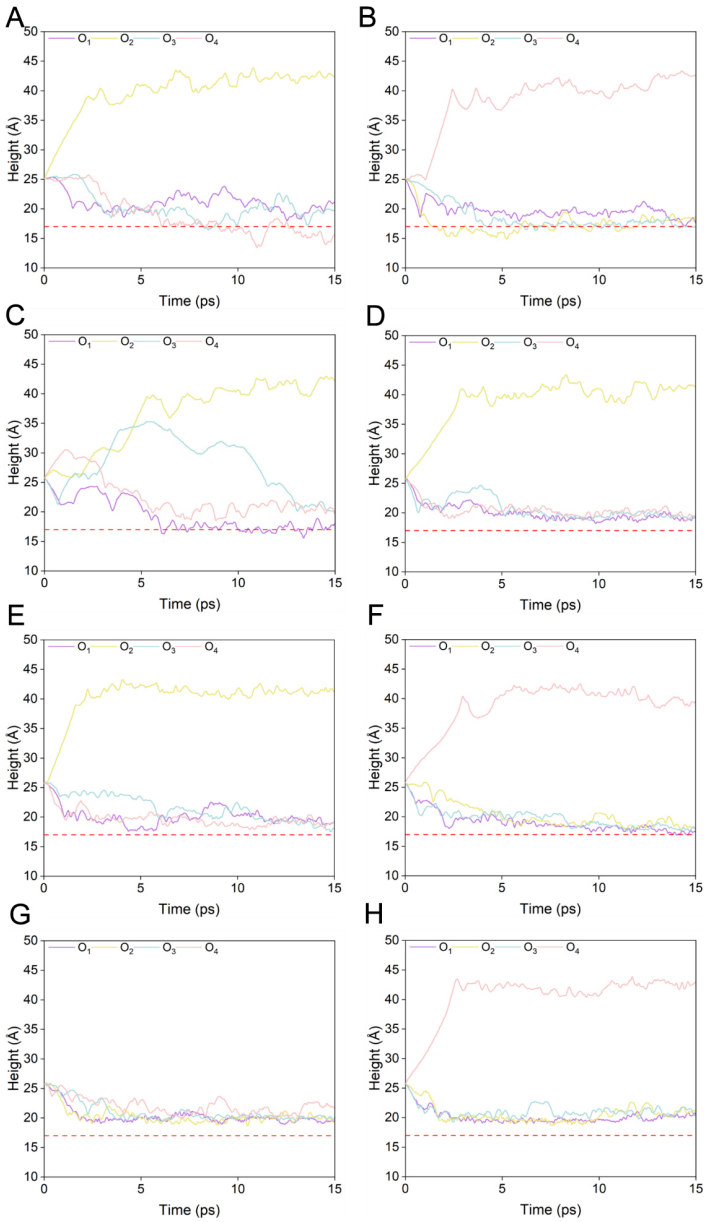


Figure 6. Height evolution of H_2O molecules in (A) Pb_I_$MAPbI_3$, (B) V_I_$MAPbI_3$, (C) APCA@Pb_I_$MAPbI_3$, (D) APCA@V_I_$MAPbI_3$, (E) APCA2OH@Pb_I_$MAPbI_3$, (F) APCA2OH@V_I_$MAPbI_3$, (G) APCA3OH@Pb_I_$MAPbI_3$, and (H) APCA3OH@V_I_$MAPbI_3$.

(2) favorable interfacial charge transfer; and (3) formation of a compact and stable electron-selective contact that effectively suppresses ion migration. These structural and electronic requirements can be fulfilled through the rational design of multifunctional PH anions, including APCA, APCA2OH, and APCA3OH. First-principles calculations and AIMD simulations reveal that the optimized APCA3OH molecule adopts a multidentate chelating configuration through cooperative Pb-O and Pb-N interactions, effectively reducing the deep and shallow trap states associated with Pb_I and V_I defects. This coordination alleviates defect-induced structural and electronic perturbations through distinct mechanisms. For the Pb_I defect, APCA3OH disrupts the Pb_3 trimer and stabilizes the resulting Pb_2 configuration, thereby substantially weakening the associated deep trap state. For the V_I defect, APCA3OH disrupts the Pb_2 dimer and restores the local inorganic octahedral framework, thereby suppressing the associated shallow trap states and reducing their electronic perturbations. Regarding the second requirement, the inherent donor-acceptor dipoles of the designed PH anions favorably tune the surface work function. This dipole effect reduces the energy-level

mismatch between the perovskite and the TiO_2 layer, decreases the effective masses of electrons and holes, and facilitates efficient carrier extraction while suppressing nonradiative recombination at the interface. Importantly, for the third requirement, the combination of strong chemical bonding and pronounced steric hindrance, particularly that introduced by the ortho-hydroxyl group in APCA3OH, increases the activation energy for iodide migration to 10.72 eV. Consequently, the passivated electron-selective contact forms a compact and robust barrier that strongly suppresses detrimental halide diffusion. Finally, this study elucidates the structure-activity relationships governing multifunctional passivation architectures. By demonstrating that targeted molecular design can simultaneously regulate defect energetics, carrier dynamics, and ion migration, this work provides a molecular design framework for constructing optimal interfacial contacts in next-generation perovskite photovoltaics.

DECLARATIONS

Acknowledgments

We are particularly grateful to associate researcher Daoxiong Wu (from Hainan University) for providing us with computing resources.

Authors' contributions

Conceptualization: Li, N.; Sun, P. P.; Chi, W.
Methodology and software: Li, N.; Sun, P. P.; Huang, J.; Dong, Q.
Investigation and formal analysis: Li, N.; Zhang, H.; Peng, Z. X; Ding, Q.
Visualization and figure preparation: Li, N.; Ding, Q.; Zhang, B.; Zhang, H.
Writing-original draft: Li, N.
Writing-review & editing: Li, N.; Sun, P. P.; Zeng, C.; Chi, W.
Funding acquisition and resources: Sun, P. P.; Chi, W.
Supervision and project administration: Sun, P. P.; Zeng, C.; Dong, Q.; Chi, W.
All authors contributed to the discussion of the results, revised the manuscript, and approved the final version.

Availability of data and materials

The original contributions presented in this study are included in the article/Supplementary Materials. Further inquiries can be directed to the corresponding author(s).

AI and AI-assisted tools statement

Not applicable.

Financial support and sponsorship

This work was supported by the National Natural Science Foundation of China (No. 52663030), the Hainan Provincial Natural Science Foundation of China (No. 225MS007), the Research Start-up Fund Project of Hainan University (No. RZ2200001216), and the Hainan Provincial Graduate Student Innovation Research Project (No. Hys2025-43).

Conflicts of interest

All authors declared that there are no conflicts of interest.

Ethical approval and consent to participate

Not applicable.

Consent for publication

Not applicable.

Copyright

© The Author(s) 2026.

Supplementary Materials

Supplementary Materials

REFERENCES

1. National Laboratory of the Rockies. Best research-cell efficiency chart. https://nrel.sitefinity.cloud/pv/cell-efficiency (accessed 2026-10-29).
2. Degani, M.; An, Q.; Albaladejo-Siguan, M.; et al. 23.7% efficient inverted perovskite solar cells by dual interfacial modification. *Sci. Adv.* **2021**, *7*, eabj7930. DOI PubMed PMC
3. Li, M.; Zhu, Z.; Wang, Z.; et al. High-quality hybrid perovskite thin films by post-treatment technologies in photovoltaic applications. *Adv. Mater.* **2024**, *36*, e2309428. DOI
4. Liu, S.; Lu, Y.; Yu, C.; et al. Triple-junction solar cells with cyanate in ultrawide-bandgap perovskites. *Nature* **2024**, *628*, 306-12. DOI
5. Duan, T.; You, S.; Chen, M.; et al. Chiral-structured heterointerfaces enable durable perovskite solar cells. *Science* **2024**, *384*, 878-84. DOI
6. Wang, Y.; Wang, F.; Song, J.; et al. Ethyl thioglycolate assisted multifunctional surface modulation for efficient and stable inverted perovskite solar cells. *Adv. Funct. Mater.* **2024**, *34*, 2402632. DOI
7. Pu, Z.; Li, J.; Xie, L.; et al. Non-fullerene acceptors assisted target therapy for interface treatment enable high performance inverted perovskite solar cells. *Small* **2024**, *20*, e2310742. DOI
8. Sun, P.; Kripalani, D. R.; Chi, W. Improved mobility and photovoltaic performance of two-dimensional ruddlesden-popper $(ThMA)_2(MA_{)2}M_3I_{10}$ perovskites applied in perovskite solar cells. *J. Alloys. Compd.* **2023**, *937*, 168464. DOI
9. Zhang, L.; Wang, Y.; Meng, X.; et al. The issues on the commercialization of perovskite solar cells. *Mater. Futures.* **2024**, *3*, 022101. DOI
10. Li, K.; Han, Y.; Zhao, X.; et al. Dual interface passivation with multi-site regulation toward efficient and stable inverted perovskite solar cells. *Adv. Energy. Mater.* **2025**, *15*, 2406046. DOI
11. Wang, S.; Sun, H.; Wang, P.; et al. Small molecule regulatory strategy for inorganic perovskite solar cells with 368 mV of V_{OC} deficit and its application in tandem devices. *Adv. Energy. Mater.* **2024**, *14*, 2400151. DOI
12. Liang, Z.; Zhang, Y.; Xu, H.; et al. Homogenizing out-of-plane cation composition in perovskite solar cells. *Nature* **2023**, *624*, 557-63. DOI PubMed PMC
13. Li, H.; Jiang, X.; Wei, Q.; et al. Low-dimensional inorganic tin perovskite solar cells prepared by templated growth. *Angew. Chem. Int. Ed.* **2021**, *60*, 16330-6. DOI
14. Lin, P.; Lin, C.; Chiu, Y.; et al. Revealing the role of thiocyanate for improving the performance of perovskite solar cells. *ACS. Appl. Energy. Mater.* **2023**, *6*, 79-88. DOI
15. Lin, P.; Loganathan, A.; Raifuku, I.; et al. Pseudo-halide perovskite solar cells. *Adv. Energy. Mater.* **2021**, *11*, 2100818. DOI
16. Kim, H.; Lim, J.; Sohail, M.; Nazeeruddin, M. K. Superhalogen passivation for efficient and stable perovskite solar cells. *Solar. RRL.* **2022**, *6*, 2200013. DOI
17. Chen, J.; Park, N. G. Nonhalide materials for efficient and stable perovskite solar cells. *Small. Methods.* **2021**, *5*, e2100311. DOI PubMed
18. Mohammed, S. O. H.; Rafiq, M.; Tahir, M.; et al. Defect passivation and crystallization regulation in wide-bandgap perovskites via p-cyanobenzenesulphonamide molecular additive. *J. Phys. Chem. Lett.* **2026**, *17*, 7465-73. DOI
19. Syed, Z. H.; Kaphan, D. M.; Perras, F. A.; et al. Electrophilic organoiridium(III) pincer complexes on sulfated zirconia for hydrocarbon activation and functionalization. *J. Am. Chem. Soc.* **2019**, *141*, 6325-37. DOI
20. Baishya, H.; Das Adhikari, R.; Patel, M. J.; et al. Synergistic modulation of buried interface and 2D-3D assisted growth of bulk via surface-functionalized layer enables > 85% fill factor in inverted perovskite solar cells. *Small* **2025**, *21*, e07345. DOI
21. Tong, X.; Ma, Y.; Xie, L.; et al. Regulating spatial charge distribution of multisite passivating additives enables stable perovskite solar cells. *Adv. Funct. Mater.* **2025**, *35*, e11458. DOI
22. Jeong, J.; Kim, M.; Seo, J.; et al. Pseudo-halide anion engineering for α-$FAPbI_3$ perovskite solar cells. *Nature* **2021**, *592*, 381-5. DOI
23. Wang, R.; Xue, J.; Wang, K. L.; et al. Constructive molecular configurations for surface-defect passivation of perovskite photovoltaics. *Science* **2019**, *366*, 1509-13. DOI
24. Yang, L.; Fang, Z.; Jin, Y.; et al. Suppressing halide segregation via pyridine-derivative isomers enables efficient 1.68 eV bandgap perovskite solar cells. *Adv. Mater.* **2024**, *36*, e2311923. DOI
25. Yang, S.; Dai, J.; Yu, Z.; et al. Tailoring passivation molecular structures for extremely small open-circuit voltage loss in perovskite solar cells. *J. Am. Chem. Soc.* **2019**, *141*, 5781-7. DOI

26. Shi, Y.; Sui, X.; He, J.; et al. Band edge engineering of lead halide perovskites using carboxylic-based self-assembled monolayer for efficient photovoltaics. *EcoEnergy* **2025**, *3*, 441-8. DOI
27. Kang, Y.; Na, S. Multi-site passivation-based antisolvent additive engineering with gradient distribution for superior triple cation P-I-N perovskite solar cells. *Nano. Energy.* **2022**, *97*, 107193. DOI
28. Li, M.; Pan, W.; Zhao, L.; et al. A multisite atomic-oxygen anchoring strategy affords efficient and stable perovskite solar cells. *Adv. Funct. Mater.* **2025**, *35*, 2413177. DOI
29. Sun, P.; Yuan, S.; Chi, W.; Cai, G. Germanium doping effect on the photoelectronic performance of alternating cations in the interlayer space $GA(MA)_3(Pb_{1-x}Ge_x)_3I_{10}$. *J. Mater. Chem. A.* **2024**, *12*, 16466-75. DOI
30. Yu, X.; Lv, Y.; Xue, B.; et al. Multiple bonding effects of 1-methanesulfonyl-piperazine on the two-step processed perovskite towards efficient and stable solar cells. *Nano. Energy.* **2022**, *93*, 106856. DOI
31. Bi, H.; Liu, J.; Wang, L.; et al. Double side passivation of phenylethyl ammonium iodide for all perovskite tandem solar cell with efficiency of 26.8%. *EcoEnergy* **2024**, *2*, 369-80. DOI
32. Jin, H. G.; Zhao, P. C.; Qian, Y.; Xiao, J. D.; Chao, Z. S.; Jiang, H. L. Metal-organic frameworks for organic transformations by photocatalysis and photothermal catalysis. *Chem. Soc. Rev.* **2024**, *53*, 9378-418. DOI PubMed
33. Guo, Z.; Xue, T.; Sun, X.; et al. Activate whole-body passivation ability of small isomeric D-π-A molecules via amino position effect to improve the photovoltaic performance of perovskite solar cells. *Chem. Eng. J.* **2023**, *452*, 139321. DOI
34. Goedecker, S.; Teter, M.; Hutter, J. Separable dual-space Gaussian pseudopotentials. *Phys. Rev. B.* **1996**, *54*, 1703-10. DOI
35. Hartwigsen, C.; Goedecker, S.; Hutter, J. Relativistic separable dual-space Gaussian pseudopotentials from H to Rn. *Phys. Rev. B.* **1998**, *58*, 3641-62. DOI
36. VandeVondele, J.; Hutter, J. Gaussian basis sets for accurate calculations on molecular systems in gas and condensed phases. *J. Chem. Phys.* **2007**, *127*, 114105. DOI PubMed
37. Kresse, G.; Furthmüller, J. Efficient iterative schemes for ab initio total-energy calculations using a plane-wave basis set. *Phys. Rev. B.* **1996**, *54*, 11169-86. DOI PubMed
38. Kresse, G.; Furthmüller, J. Efficiency of ab-initio total energy calculations for metals and semiconductors using a plane-wave basis set. *Comput. Mater. Sci.* **1996**, *6*, 15-50. DOI
39. Kresse, G.; Hafner, J. Ab initio molecular dynamics for liquid metals. *Phys. Rev. B.* **1993**, *47*, 558-61. DOI
40. Perdew, J. P.; Burke, K.; Ernzerhof, M. Generalized gradient approximation made simple. *Phys. Rev. Lett.* **1996**, *77*, 3865-8. DOI PubMed
41. Blöchl, P. E. Projector augmented-wave method. *Phys. Rev. B.* **1994**, *50*, 17953-79. DOI
42. Henkelman, G.; Uberuaga, B. P.; Jónsson, H. A climbing image nudged elastic band method for finding saddle points and minimum energy paths. *J. Cheml. Phys.* **2000**, *113*, 9901-4. DOI
43. Henkelman, G.; Jónsson, H. Improved tangent estimate in the nudged elastic band method for finding minimum energy paths and saddle points. *J. Chem. Phys.* **2000**, *113*, 9978-85. DOI
44. Grimme, S. Semiempirical GGA-type density functional constructed with a long-range dispersion correction. *J. Comput. Chem.* **2006**, *27*, 1787-99. DOI PubMed
45. Vandevondele, J.; Krack, M.; Mohamed, F.; Parrinello, M.; Chassaing, T.; Hutter, J. Quickstep: fast and accurate density functional calculations using a mixed Gaussian and plane waves approach. *Comput. Phys. Commun.* **2005**, *167*, 103-28. DOI
46. Hutter, J.; Iannuzzi, M.; Schiffmann, F.; Vandevondele, J. cp2k: atomistic simulations of condensed matter systems. *WIREs. Comput. Mol. Sci.* **2014**, *4*, 15-25. DOI
47. Hoover, W. G. Constant-pressure equations of motion. *Phys. Rev. A.* **1986**, *34*, 2499-500. DOI
48. Nosé, S. A unified formulation of the constant temperature molecular dynamics methods. *J. Chem. Phys.* **1984**, *81*, 511-9. DOI
49. Lu, T.; Chen, F. Multiwfn: a multifunctional wavefunction analyzer. *J. Comput. Chem.* **2012**, *33*, 580-92. DOI
50. Agiorgousis, M. L.; Sun, Y. Y.; Zeng, H.; Zhang, S. Strong covalency-induced recombination centers in perovskite solar cell material $CH_3NH_3PbI_3$. *J. Am. Chem. Soc.* **2014**, *136*, 14570-5. DOI PubMed
51. Yin, W.; Shi, T.; Yan, Y. Unusual defect physics in $CH_3NH_3PbI_3$ perovskite solar cell absorber. *Appl. Phys. Lett.* **2014**, *104*, 063903. DOI
52. Haruyama, J.; Sodeyama, K.; Han, L.; Tateyama, Y. First-principles study of ion diffusion in perovskite solar cell sensitizers. *J. Am. Chem. Soc.* **2015**, *137*, 10048-51. DOI PubMed
53. Azpiroz, J. M.; Mosconi, E.; Bisquert, J.; De Angelis, F. Defect migration in methylammonium lead iodide and its role in perovskite solar cell operation. *Energy. Environ. Sci.* **2015**, *8*, 2118-27. DOI
54. Gao, F.; Zhao, Y.; Zhang, X.; You, J. Recent progresses on defect passivation toward efficient perovskite solar cells. *Adv. Energy. Mater.* **2020**, *10*, 1902650. DOI

55. Ball, J. M.; Petrozza, A. Defects in perovskite-halides and their effects in solar cells. *Nat. Energy.* **2016**, *1*, BFnenergy2016149. DOI
56. Sun, J.; Liu, N.; Wang, D.; Li, Q.; Qiu, F. Maximizing defect formation energies via collaborative passivation achieves high-performance perovskite solar cells. *ACS. Appl. Mater. Interfaces.* **2025**, *17*, 67926-33. DOI
57. Qin, T.; Wu, F.; Ma, D.; et al. Asymmetric sulfonyldibenzene-based hole-transporting materials for efficient perovskite solar cells: inspiration from organic thermally-activated delayed fluorescence molecules. *ACS. Materials. Lett.* **2020**, *2*, 1093-100. DOI
58. Ganesan, P.; Chen, D.; Chen, W.; et al. Methoxy substituents activated carbazole-based boron dimesityl TADF emitters. *J. Mater. Chem. C.* **2020**, *8*, 4780-8. DOI
59. Dou, B.; Whitaker, J. B.; Bruening, K.; et al. Roll-to-roll printing of perovskite solar cells. *ACS. Energy. Lett.* **2018**, *3*, 2558-65. DOI
60. Shi, Y.; Zhang, Y.; Wen, J.; et al. Interpretable machine learning for stability and electronic structure prediction of Janus III-VI van der Waals heterostructures. *Mater. Genome. Eng. Adv.* **2024**, *2*, e76. DOI
61. Liu, Z.; Liu, T.; Li, M.; et al. Eliminating halogen vacancies enables efficient MACL-assisted formamidine perovskite solar cells. *Adv. Sci.* **2024**, *11*, e2306280. DOI
62. Temitmie, Y. A.; Haider, M. I.; Cuzzupè, D. T.; et al. Overcoming the open-circuit voltage losses in narrow bandgap perovskites for all-perovskite tandem solar cells. *ACS. Mater. Lett.* **2024**, *6*, 5190-8. DOI PubMed PMC
63. Ausman, G. A.; Mclean, F. B. Electron-hole pair creation energy in SiO_2. *Appl. Phys. Lett.* **1975**, *26*, 173-5. DOI
64. Scholze, F.; Rabus, H.; Ulm, G. Measurement of the mean electron-hole pair creation energy in crystalline silicon for photons in the 50-1500 eV spectral range. *Appl. Phys. Lett.* **1996**, *69*, 2974-6. DOI
65. Wang, G.; Chu, H.; Deng, K.; et al. Metal effect boosts the photoelectric properties of two-dimentional Dion-Jacobson (3AMPY)$(MA)_3M_4I_{13}$ perovskites. *J. Colloid. Interface. Sci.* **2025**, *692*, 137493. DOI
66. Wang, G.; Wu, J.; Deng, K.; et al. Mechanistic pathways in the photocatalytic CO_2 reduction on halide double perovskite Cs_2NaBiX_6 (X = Cl/Br/I). *J. Catal.* **2025**, *449*, 116228. DOI
67. Zhang, L.; Miao, H. Application of the transformed differential quadrature method to the free vibration analysis of photoelectrically loaded perovskite annular plates with an eccentric hole. *Thin-Walled. Struct.* **2025**, *216*, 113593. DOI
68. Yan, L.; Wang, M.; Zhai, C.; Zhao, L.; Lin, S. Symmetry breaking induced anisotropic carrier transport and remarkable thermoelectric performance in mixed halide perovskites $CsPb(I_{1-x}Br_x)_3$. *ACS. Appl. Mater. Interfaces.* **2020**, *12*, 40453-64. DOI
69. Li, X.; Meng, Y.; Li, W.; et al. Multislip-enabled morphing of all-inorganic perovskites. *Nat. Mater.* **2023**, *22*, 1175-81. DOI
70. Wu, J.; Wang, G.; Ding, Q.; et al. Atomic-level insights from DFT calculations guide the design of metal ion-doped 2D $GA(MA)_3Pb_3I_{10}$ perovskites for enhanced photocatalytic CO_2 reduction. *Appl. Surf. Sci.* **2026**, *727*, 166047. DOI
71. Lu, T. A comprehensive electron wavefunction analysis toolbox for chemists, Multiwfn. *J. Chem. Phys.* **2024**, *161*, 082503. DOI
72. Liu, Z.; Lu, T.; Chen, Q. An sp-hybridized all-carboatomic ring, cyclo[18]carbon: Electronic structure, electronic spectrum, and optical nonlinearity. *Carbon* **2020**, *165*, 461-7. DOI
73. Lian, C.; Ali, Z. A.; Kwon, H.; Wong, B. M. Indirect but efficient: laser-excited electrons can drive ultrafast polarization switching in ferroelectric materials. *J. Phys. Chem. Lett.* **2019**, *10*, 3402-7. DOI PubMed
74. Lee, T.; Park, H.; Joo, S.; et al. Hydrogen-rich argyrodite solid electrolytes for NCM/Li all-solid-state batteries. *ACS. Energy. Lett.* **2024**, *9*, 4493-500. DOI
75. Deng, K.; Wang, G.; Song, J.; et al. Carboxylate pseudohalide anions for enhanced defect mitigation and stability of $MAPbI_3$ perovskite. *Energy. Mater. Adv.*. DOI
76. Wang, J.; Duan, X. Unveiling the role of surface iodine vacancies in $CsPbI_3$ perovskite: carrier recombination dynamics and defect passivation mechanisms. *Inorg. Chem. Front.* **2025**, *12*, 569-77. DOI
77. Li, Q.; Tao, H.; Zhang, C.; et al. Passivation of iodine vacancies in perovskite photodetectors by oxygen functional groups in the main and side chains of alcohol polymers. *ACS. Appl. Electron. Mater.* **2025**, *7*, 884-90. DOI
78. Wu, P.; Zhang, X.; Zhang, K.; et al. Ti_2CT_x-MXene as an efficient passivation layer to regulate the vertical growth of perovskite layers and enhance the performance of solar cells. *ACS. Appl. Mater. Interfaces.* **2025**, *17*, 12095-104. DOI
79. Bastolla, U. Computing protein dynamics from protein structure with elastic network models. *WIREs. Comput. Mol. Sci.* **2014**, *4*, 488-503. DOI
80. Xu, K.; Bu, H.; Pan, S.; et al. GPUMD 4.0: a high-performance molecular dynamics package for versatile materials simulations with machine-learned potentials. *Mater. Genome. Eng. Adv.* **2025**, *3*, e70028. DOI

Disclaimer/Publisher's Note: All statements, opinions, and data contained in this publication are solely those of the individual author(s) and contributor(s) and do not necessarily reflect those of OAE and/or the editor(s). OAE and/or the editor(s) disclaim any responsibility for harm to persons or property resulting from the use of any ideas, methods, instructions, or products mentioned in the content.

© The Author(s) 2026. Open Access This article is licensed under a Creative Commons Attribution 4.0 International License (https://creativecommons.org/licenses/by/4.0/), which permits unrestricted use, sharing, adaptation, distribution and reproduction in any medium or format, for any purpose, even commercially, as long as you give appropriate credit to the original author(s) and the source, provide a link to the Creative Commons license, and indicate if changes were made.